ELSEVIER

Scattered wave imaging of the lithosphere–asthenosphere boundary

Catherine A. Rychert [a],[*], Peter M. Shearer [a], Karen M. Fischer [b]

[a] *Institute of Geophysics and Planetary Physics, Scripps Institution of Oceanography, University of California, San Diego, 9500 Gilman Drive M/C 0225, La Jolla, California 92093, United States*
[b] *Department of Geological Sciences, Brown University, 324 Brook Street, Box 1846, Providence, Rhode Island 02912, United States*

ARTICLE INFO

ABSTRACT

Several recent studies have imaged discontinuities interpreted as the lithosphere–asthenosphere boundary using receiver function methods. These are exciting results since this boundary is fundamental and yet relatively elusive. Its location is not well imaged nor are its properties well understood. The receiver function method provides high depth resolution, and the multitude of studies using this method have increased lateral resolution. A better global understanding of the location and nature of the boundary is developing, which ultimately will have implications for mantle dynamics and planetary evolution. However, these new results do not all form a clear and consistent picture, and in some cases introduce new complexities and questions. Some apparent contradictions may represent unmodeled Earth structure. Overall, interpretation and synthesis requires careful consideration of the approaches and sensitivities of individual studies.

© 2009 Elsevier B.V. All rights reserved.

1. Introduction

The Earth's tectonic plates are made of the crust and some amount of mantle. However, how much mantle constitutes a plate is not precisely known, nor are all of the properties that distinguish the coherent plate from the rest of the mantle. Plate tectonic theory hinges on the existence of a transition from a rigid plate, or lithosphere, to a weaker layer below, the asthenosphere. The nature of the boundary between the conducting lid and the convecting mantle has broad implications. For instance, a sharp contrast in viscosity will affect how the plates couple to deeper mantle flow, and the location of such a boundary may modulate overall convection patterns. A better understanding of mantle dynamics has implications for the general evolution of the lithosphere, the mechanisms and conditions of continent formation, and reasons for craton stability versus erosion.

Despite its important implications, our understanding of this fundamental boundary is limited in comparison to other interfaces in the Earth. Several other boundaries are relatively well-mapped seismically, with general agreement among studies using a variety of methods, data, and disciplines regarding the mechanisms that define them, and broad correlations between the depths of the boundaries and tectonic environment. For instance the Moho, a compositional boundary, is well imaged at 6–9 km depth beneath the oceans and at 25–45 km beneath most continental regions. Interior to the continents the boundary is often shallower beneath rifts and deeper beneath orogenic belts (e.g., Christensen and Mooney, 1995). There is similar agreement that the 410 and 660 km discontinuities represent phase changes, and the depths to the boundaries vary according to the thermal variations caused by tectonic features such as subducted slabs or plumes.

The lithosphere–asthenosphere boundary has been described using data from seismic, electromagnetic, gravity, geochemical, and heat flow studies. General agreement exists that the boundary increases in depth from average ocean to average continent, but that is the extent of consensus and tectonic correlation. There is not necessarily a relationship between the thickness of lithosphere and that of the crust (e.g., Rychert and Shearer, 2009), nor is the deepest lithosphere always located beneath the oldest Archean environments, e.g., Australia (Simons et al., 1999; Fishwick et al., 2005; Fishwick et al., 2008). The boundary is thought to be defined by some combination of depletion, dehydration, grain size, partial melting, temperature, or anisotropic orientation or intensity (Jordan, 1978; Anderson, 1989; Hirth et al., 2000; Gung et al., 2003; Karato, 2003; Faul and Jackson, 2005; Marone et al., 2007; Kobussen et al., 2008). In other words, it is not known what mechanism(s) defines the boundary, or even if there is one single global mechanism or a combination of mechanisms.

One classic definition of the lithosphere is the outer layer of the Earth capable of withstanding deviatoric stress over geologic time-scales, whereas the asthenosphere is the more plastic layer below where isostatic adjustment occurs (Jordan, 1978). However, definitions of lithospheric strength and its relationship to isostatic adjustment are debated, and vary with the scales of deformation in space and time (e.g., Forsyth, 1985; McKenzie and Fairhead, 1997; Peltier and Drummond, 2008). For the purposes of this paper, we will use the term lithosphere–asthenosphere boundary to refer to a drop

---

in seismic wavespeed, shear-wave velocity in particular, that corresponds to a drop in the elastic shear strength of the mantle. Seismic imaging of the boundary adds important constraints since seismic waves are affected by all of the mechanisms listed above that may distinguish the lithosphere from the asthenosphere, and some of the mechanisms have unique effects on the waveforms. In addition, seismic waves have the potential to image the boundary over large swaths of the mantle, and within and across various tectonic settings at a resolution high enough to answer questions regarding the properties that define the plate.

2. Seismic constraints other than receiver functions

Global tomography images an increase in seismic velocity from ocean to craton in the depth range of 150–250 km at broad wavelengths of ~1000 km, which is generally thought to be evidence for the thickening of the seismically fast lid (Kustowski et al., 2008; Lebedev and van der Hilst, 2008; Nettles and Dziewonski, 2008). However, finer scale variability is not well mapped and the boundary may be more complex. Attaining high-resolution imaging in the depth range of the lithosphere–asthenosphere boundary has proven challenging with existing seismic data and techniques. Regional tomography results indicate that the depth of the lithosphere–asthenosphere boundary likely varies at a finer scale than the resolution of global tomographic studies. Yet regional surface-wave tomography is limited to a resolution of 100 s of km laterally and 40–50 km vertically. In addition, surface-wave resolution decreases at depth, and thus these waveforms have the potential to underestimate or overestimate lithospheric thickness. Regional body-wave tomography can resolve finer scale lateral features but suffers from vertical smearing.

ScS reverberations and multiple bounce S waves can put tighter constraints on the depth range over which shear-wave velocity discontinuities occur. Beneath the old Pacific plate, ScS reflectivity profiles were used to constrain a 5.6–6.4% velocity drop that occurs over <30 km at ~68 km depth (63 km depth beneath the ocean floor) (Gaherty et al., 1999). For the entire Pacific plate a study using ScS reverberations found a 4.7–14.3% velocity drop that occurs over <10–15 km at 80 km depth (Bagley and Revenaugh, 2008), and a study using multiple S bounces found similarly strong sharp drops, i.e., a 7.8–9.2% decrease from 66 to 163 km, with 5.6–5.9% occurring at 66 km (Tan and Helmberger, 2007). These velocity drops are typically imaged at a relatively constant depth, and have been interpreted as the base of the melt-separation zone, i.e., frozen-in structure related to lithospheric formation at the ridge (Gaherty et al., 1999), rather than the lithosphere–asthenosphere boundary defined only by plate-cooling, which would increase in depth with distance from the ridge. Very low velocities beneath the lid have also been interpreted as requiring partial melting in the deeper layer (Tan and Helmberger, 2007). Results beneath continents from these studies include a velocity drop beneath eastern China (Revenaugh and Sipkin, 1994), and the absence of an apparent velocity drop with depth beneath Australia (Gaherty et al., 1999).

Higher frequency studies, such as reflection and refraction seismology, can image structure at a finer scale than that resolvable by regional tomography and longer period seismic stacks. These experiments generally involve active sources, i.e., nuclear or chemical explosions or airguns. Results from the longest arrays reach depths associated with the lithosphere–asthenosphere boundary. Most are continental, and generally reveal structures of higher complexity. Velocity decreases with depth at ~100 km have been observed beneath Siberia, Europe, North America, and Australia (Pavlenkova et al., 2002; Thybo, 2006) and interpreted as small amounts of partial melting (Thybo, 2006). The Urals Seismic Experiment and Integrated Studies found reflectors at 100, 140–160 and 225 km, which were interpreted as either mafic intrusions, internal faults, or shear-related rheologic layering at the lithosphere–asthenosphere boundary (Steer et al., 1998). Beneath the Quartz array the lithosphere–asthenosphere boundary has been interpreted as

dipping from 120–150 km beneath the Altay-Sayan fold belt to 200–220 km beneath the Baltic Shield with a more complex, mid-lithospheric, low-velocity zone (Ryberg et al., 1996; Morozova et al., 2000). The MONA LISA Working Group found a boundary from 50 km beneath the Central Graben to 100 km beneath the Baltic Shield that was interpreted as a sharp rheologic lithosphere–asthenosphere boundary (MONA LISA Working Group, 1997). More in depth reviews of these results are given in the work of Bostock (1999) and Thybo (2006).

Overall, the difference between a seismically fast lid and a slower asthenosphere is imaged in most regions at a global or regional scale (e.g., Nishimura and Forsyth, 1989; Li et al., 2003; Li and Burke, 2006; Kustowski et al., 2008; Nettles and Dziewonski, 2008) at a resolution at which the boundary could be defined by a wide variety of physical or chemical properties. In some local to regional scale studies sharper boundaries have been imaged, and these are sometimes interpreted as the lithosphere–asthenosphere boundary. However, attempts to image the boundary using body waves stacked at a global and regional scale have failed (Shearer, 1991). What makes the depth and character of this fundamental boundary elusive? To be imaged by regional and global surface-wave studies but not body-wave stacks over approximately the same spatial area the boundary must either be diffuse and/or vary laterally in depth and/or character.

3. Receiver functions: disadvantages, advantages

Ps and Sp receiver functions offer additional constraints. Ps refers to a teleseismic compressional waveform that converts to a shear-wave at a seismic velocity discontinuity, a change in velocity with depth beneath a seismic station, whereas Sp is a shear-wave that converts to a compressional wave. The waveforms originate from earthquakes at epicentral distances ~35–80° (Ps) and ~55–80° (Sp) away from the station. Ps and Sp converted waveforms are both primarily sensitive to shear-wave velocity discontinuities, which can be imaged using receiver function techniques (e.g., Rychert et al., 2007). These methods generally rotate the recorded wavefield into its P and SV components using either the theoretical angle of rotation (Bostock, 1998) or one that is derived empirically by minimizing P energy on the S waveform and vice versa (e.g. Kumar et al., 2005b). The source waveform (P for Ps and S for Sp) is then deconvolved from the converted component waveform (S for Ps and P for Sp). This is done either iteratively in the time domain (Ligorria and Ammon, 1999) or in the frequency domain (Bostock, 1998). The resulting deconvolved waveform corresponds to the shear-wave component of Earth's impulse response. Positive phases correspond to velocity increases with depth, and negative phases to velocity decreases, and absolute amplitude corresponds to the magnitude of the velocity drop. Sp has polarity opposite that of Ps, but is generally presented inverted so that polarities correspond to those of Ps. Delay time with respect to the source waveform corresponds to conversion depth, and waveforms are typically migrated, i.e., scaled to depth assuming a velocity model. Discontinuities that are not perfectly sharp increase pulse widths and decrease amplitudes, and the magnitude of this effect depends on the dominant period of the incident waveform. Here we have only described the simple 2-D isotropic case assuming a horizontal interface (i.e. no dip), but note that Ps and Sp converted waveforms may also be created at anisotropic interfaces and dipping interfaces, which produce back-azimuthal variations in amplitude. Ps and Sp receiver functions have some limitations, but also several advantages, both of which we describe below.

Ps receiver functions are complicated by crustal reverberations, which have the potential to obscure impulse responses down to depths of ~200 km. In addition low-pass filtering, which is required for Ps and Sp in the absence of sufficient quantities of high quality data, increases interference of phases of interest with other phases. In the past, low-pass filtering of Ps reverberations has obscured fine-scale structure in the depth range of the lithosphere–asthenosphere boundary. Sp is not complicated by crustal reverberations, since direct

conversions arrive before the source phase, and reverberations arrive afterwards. However, Sp is noisy in comparison to Ps. Therefore, clear Sp signals generally require data collection over longer time periods. Sp is also longer period, and so lower resolution. Finally, receiver function results are usually limited to local to regional scales since they only give information about structure from a circular region surrounding the seismic station at depth.

Yet, Ps and Sp have the potential to image sharp boundaries at high resolution over large lateral swaths without the need for active source imaging. Many recent studies have used receiver function techniques to image seismic discontinuities in the upper mantle that may be associated with the lithosphere–asthenosphere boundary. These new results are clearer owing to larger quantities of data at global seismic stations and increases in the number of new seismic arrays. Profusion of data means that data stacking can be used to increase signal-to-noise rather than low-pass filtering, so that higher resolution is attained. High lateral resolution, which primarily comes from arrays, is important for mapping depth and/or character variations in the interface, especially at tectonic boundaries. High depth resolution is important for constraining the sharpness of the associated velocity contrast, and thus the mechanism that defines the boundary. A gradual velocity drop may be defined by thermal gradients alone, but a sharp contrast requires another mechanism, such as compositional change or melting.

For instance, beneath eastern North America Ps and Sp analysis imaged a sharp boundary (Rychert et al., 2007) that was within the gradual drop in velocity from the lid to the layer below from surface-wave studies (van der Lee, 2002; Li et al., 2003). Modeling the seismic velocity gradient associated with the observed converted phase constrained a sharp velocity contrast (5–10% over less than 11 km depth). The gradient was too sharp to be defined by thermal gradients alone, requiring a mechanism such as depletion and dehydration possibly in combination with an anisotropic component, or partial melting in the asthenosphere. Ps and Sp imaging have the potential to resolve the mechanism that defines velocity discontinuities, which is one reason for the focus on high-resolution phases.

In terms of lateral resolution, Ps and Sp phases give information from a small ring below the station. At about 100 km depth Ps phases are converted from a radius ~20–40 km horizontally away from the station vs. ~100 to several hundred km for Sp. Resolution depends on event and station distributions. Ps and Sp coverage is far from global. One recent study considered Ps single-station results systematically globally (Rychert and Shearer, 2009). Complications from reverberations eliminated many stations from the global study, but a strong negative phase was identified at all locations where crustal phases could also be clearly identified, indicating a velocity discontinuity at 60–110 km depth range. The average depth to the phase varies from 70±4 km beneath Phanerozoic oceans, to 81±2 km beneath Phanerozoic orogenic/magmatic zones, to 95±4 km beneath Precambrian shields and platforms (Jordan, 1981). The depths fall within the gradual drops in velocity from tectonically averaged global surface-wave models (Nettles and Dziewonski, 2008), and the imaged phases likely represent the lithosphere–asthenosphere boundary in most locations. However, beneath Precambrian shields and platforms the Ps depth (95 km) is too shallow to be the base of the fast cratonic lid, which extends to 200–250 km depth. Indeed, beneath individual stations in Precambrian tectonic environments Ps depths are shallower than the gradual drop in surface-wave velocity profiles with depth. In these regions the Ps conversions seen in the global study likely represent the edges of cratons or frozen-in fabric, both of which will be discussed in later sections.

The numerous recent receiver publications that interpret a lithosphere–asthenosphere boundary lend new insight, though in some cases accompanied by increased complexity. We will attempt to put these results in context by reviewing recent progress in receiver function imaging of seismic discontinuities interpreted to be the lithosphere–asthenosphere boundary, and discuss implications for the mechanism that defines the boundary.

4. Receiver function imaging of the lithosphere–asthenosphere boundary

This section reviews receiver function results related to the lithosphere–asthenosphere boundary; more details can be found in Table 1.

In oceanic environments, velocity decreases with depth interpreted as the lithosphere–asthenosphere boundary have been reported from stations on or buried near ocean islands at 40–140 km depth. Beneath Hawaii both Ps and Sp image a drop in this range (Li et al., 2000; Collins et al., 2002; Li et al., 2004; Wolbern et al., 2006) deepening from Kauai (50–60 km) to Oahu (65–90 km) to the Big Island (90–140 km). Velocity deceases interpreted as the lithosphere–asthenosphere boundary at a similar depth range have been reported in the North Atlantic, for Iceland (80 km), eastern and western Greenland (70 km and 100–120 km), and Jan Mayan (40–60 km) (Kumar et al., 2005a). Similarly, lithosphere–asthenosphere boundary depths have been reported beneath the Galapagos (70 km) and Easter Island (50 km) (Heit et al., 2007) and islands in the Indian Ocean (80 km) (Kumar et al., 2007). The global Ps average for ocean island stations is 70±4 km (Rychert and Shearer, 2009). Oceanic lithosphere is ideal for testing theories regarding the properties that define the lithosphere–asthenosphere boundary given its relatively simple structure and tectonic history in comparison to continents. However, broader interpretation of the aforementioned results from ocean islands is complicated by the fact that these locations may represent anomalous hot-spot environments, i.e. they may not be well suited for testing hypotheses regarding lithospheric thickening with age or the mechanism that defines typical, unaltered oceanic lithosphere.

Receiver function imaging of typical oceanic lithosphere, i.e., that not on islands and/or altered by hotspots, has proven challenging. Ocean floor sediment layers have strong impedance contrasts which cause significant ringing, generally eliminating the possibility of detecting phases from deeper discontinuities using instruments deployed directly on the ocean floor (Harmon et al., 2007). However, one recent receiver function study used two borehole instruments to avoid sediment reverberations and to estimate the depth of the lithosphere–asthenosphere boundary using Ps and Sp phases (Kawakatsu et al., 2009). This study found lithospheric thickening with age: from 55 km and 76 km depth in 25 My-old and 49 My-old lithosphere on the Philippine Sea Plate to 82 km depth in 129 My-old Pacific Plate lithosphere, although the Pacific Plate receiver function was relatively noisy. The station on the Philippine Sea Plate was stacked in two common conversion point bins to get depths at two different lithospheric ages. The study concluded that the high frequencies of the waveforms (3 s) require a strong, sharp lithosphere–asthenosphere boundary, defined by asthenospheric melting.

Receiver functions have imaged seismic velocity discontinuities interpreted to be the lithosphere–asthenosphere boundary beneath many continental regions with thin lithosphere (65–120 km) including eastern and western North America (90–110 km) (Rychert et al., 2005; Li et al., 2007; Rychert et al., 2007), the Tanlu fault zone and the Bohai Bay Basin (60–80 km), the Taihang Mountains (120 km), the central North China Craton (90 km), (Chen et al., 2006; Chen et al., 2008; Chen, 2009) and the Dabie Shan (60–72) (Sodoudi et al., 2006b) in China, the Tien Shan (90–120 km) (Oreshin et al., 2002; Kumar et al., 2005b), the Dead Sea (80 km), Gulf of Arabia (65 km), Turkey (65–90 km), the Arabian Shield (50–120 km) (Angus et al., 2006; Mohsen et al., 2006; Hansen et al., 2007; Ozacar et al., 2008), Central Albortz (90 km) (Sodoudi et al., 2009), northern Africa and Crete (100 km) (Sodoudi et al., 2006a), the Dharwar Craton (80–100 km) (Kumar et al., 2007), northeastern and coastal Brazil (80 km) and southern Brazil (120 km) (Heit et al., 2007). Most of these shallow discontinuities are located either on Phanerozoic orogenic/magmatic zones or Phanerozoic platforms (Jordan, 1981).

Table 1

Compilation of receiver function results that find velocity decreases with depth or changes in anisotropic orientation between the Moho and 300 km depth. Numbered references interpret results as the lithosphere–asthenosphere boundary and are included in the global compilation in Fig. 1 with locations indicated by corresponding numbers. Lettered references find velocity decreases with depth or changes in anisotropy that are not necessarily interpreted as the lithosphere–asthenosphere boundary. The locations of the lettered results are included in Fig. 1, but the results are not included in the global compilations in Figs. 1 and 2. The symbol (a, b, or c) in the reference column refers to the values used in the compilations (Figs. 1 and 2), while the symbol in the depth summary column refers to the values in that column. The approximate latitude and longitude values in column 2 are presented to give a general overview of the locations of individual studies. They are not necessarily those used in Fig. 1, since Fig. 1 contains higher resolution information. For studies that considered multiple data sets, each set is listed in the data column separated by the ; symbol.

Reference	Region	Method	Data	Depth summary (km)	Modeling and/or interpretation
	Approximate latitude	Data, stacking, domain	station or array (# stations)[e] running time[e]		
	Approximate longitude				
1. Li et al., (2000)[c]	Hawaii–Oahu Lat 18.5–22 Lon −159 to −154	Ps, CSS and regional, time	array HBSN (6)[f]; perm. sta. KIP	130–140[c] Big Island 90[c] Oahu KIP	~10–20% step-function-like
2. Li et al., (2004)[c]	Hawaii–Oahu Lat 18–23 Lon −160 to −152	Sp, CCP, time	perm. stas. POA, MAUI, KIP	100–110[c] Big Island 50–60[c] Kauai	
3. Collins et al. (2002)[c]	225 km SW of Oahu Lat 19.5 Lon −159.25	Ps, CSS, freq.	buried sta. OSN1, 4 months	80[c]	~15–20%, step function
4. Wolbern et al. (06)[c]	Hawaii Lat 18.5–22.5 Lon −160 to −154	Ps, CSS and CCP, time	Hawaii plume project (11) 2 years; stas. POA, MAUI, KIP, MIDW; temp. stas. KHU, STC, UXL; array HIBSN	90[c] Big Island 65[c] Oahu	
5. Heit et al. (2007)[a]	South America Lat −10 to −60 Lon −40 to −20	Sp, CSS and larger regional bins, time	arrays BLSP, ReFuCA, BANJO; perm. stas. (14)	160[a] central Brazil 130[a] Amazonas, Brazil 140[a] Falkland Islands 120[a] S Brazil 80[a] N.E. Brazil and coast 70[a] Galapagos, French Guyana 50[a] Easter Island	
6. Li et al. (2007)[b]	W. U.S. Lat 32–48 Lon −125 to −110	Sp, CCP, time	perm. stas. (67)	~70[c] average 60–100[b] overall	over <20 km melt at ~100 km
7. Rychert et al. (2005)[c]	E. U.S. Lat 40–49 Lon −80 to −64	Ps, CSS, freq.	perm. stas. HRV, LMN, PAL, BINY, SSPA, LBNH, 5–14 years	90–110[c]	3.1–11% over <11 km
8. Rychert et al. (2007)[c]	E .U.S. Lat 40–50 Lon −80 to −62	Ps and Sp, CSS, freq.	perm stas. HRV, LMN, 14 years, 10 years	87–105[c]	5–10% over <11 km
9. Snyder (2008)[b]	Slave craton Lat 63–67 Lon –115 to –110	Ps, CSS, freq.	POLARIS Slave Array (20) 3–5 years	190–220[b]	
A. Bostock (1998)	Slave province Lat 62–62.5 Lon −114 to −115	Ps, CSS, freq.	array YKA (4) ~9 years; sta. RSNT ~3 years	70–80[c] 120–150[c] 170–230[c] dip towards Slave 350[c] (isotropic)	Anisotropic layering and dense silicate melt fraction
B. Mercier et al. (2008)	Northwestern Canada, Wopmay orogen and western Slave Lat 61–62.25 Lon −123 to −116	Ps, CSS, freq.	array CANOE (20) ~2 years	30–90[c] dip toward continental interior (east)	fine-scale anisotropic mantle layering related to fossil subduction
C. Yuan et al., (2006)	Slave province Lat 62.56 Lon −114.6	Sp[d], CSS, time	sta. YKW3, ~16 years	120[c]	
10. Kumar et al. (2005a)[b]	N. Atlantic Lat 60–90 Lon 0 to −75	Sp, CCP, time	arrays GLATIS, NEAT, ICEMELT, HOTSPOT, months-years; perm. IRIS and GEOFON stas.; stas. JMI, JMIC	40–60[c] Jan Mayan 100–120[c] W. Greenland 80[c] Iceland and large parts of Greenland 70[c] E. Greenland	
D. Vinnik et al. (2005)	Iceland Lat 63.5–66.5 Lon −24 to −13	Sp, CCP, time	arrays Iceland Hotspot Project, ICEMELT, and SIL (58)	80±5[c] Iceland 135±5[c] peripheral Iceland	Dry harzburgite to wet peridotite
E. Farra and Vinnik (2000)[c]	S.W. German Basin Lat 48.5–49.75 Lon 11–12	Ps and Sp, CSS, time	array GRF (3) ~13–20 years	80[c] (anisotropy)	Change in direction of azimuthal anisotropy
11. Sodoudi et al. (2006b)[a]	Aegean Lat 34–42 Lon 19–29	Sp[d], CCP, time	array Seisfaultgreece (22) 6 months; perm. GEOFON stas. (8) ~10 years; sta. MEDNET; perm. National Observatory of Athens stas. (21) ~3 years; temp. array CYC-NET (22) 2 years	100[c] Crete (African lith.) 225[c] beneath arc 150[c] (Agean lith.)	

Table 1 (*continued*)

Reference	Region	Method	Data	Depth summary	Modeling and/or
	Approximate latitude	Data, stacking, domain	station or array (# stations)[e] running	(km)	interpretation
	Approximate longitude		time[e]		
12. Ozacar et al. (2008)[c]	Turkey Lat 37–41.5 Lon 37–44	Ps, CCP, time	array ETSE (29) ~22 months	65[c]	
13. Angus et al. (2006)[b]	Arabian and Eurasian collision zone in E. Turkey Lat 37–42 Lon 37–46	Sp, CCP, freq.	array ETSE (29) ~22 months; perm. stas. GNI, MALT	60–80[c] E. Turkey 100–125[c] Arabian Shield and Iranian Plateau	
14. Mohsen et al. (2006)~	Dead Sea Transform, E. Turkey, Arabian Peninsula Lat 23–39 Lon 30–46	Sp, CSS, and CCP, time	DESERT (22) 1 year; perm. stas. KEG, JER, CSS, EIL, RAYN, MALT	80[c] Dead Sea 65[c] Gulf of Arabia 90[c] E. Turkey 160[c] Arabian Shield	
15. Hansen et al. (2007)[a]	Arabian Peninsula Lat 15–35 Lon 35–55	Sp, CSS, time	SANDSN (27) ~7 years; Saudi Arabian Broadband Array (8) ~18 months; stas. (4) ~1 – 3 years	50–120[b] Arabian Shield 160[b] Arabian Platform	
F. Vinnik et al. (2004)	Arabia (Gulf of Eden) Lat 11–16 (ATD 11.5) Lon 43–50 (ATD 42.8)	Sp, CSS, time	sta. ATD	160[c]	Onset of melting
G. Levin and Park (2000)	Arabian Shield Lat 23.5 Lon 45.5	Ps, CSS, freq.	sta. RAYN, ~2.5 years	70[c]	Anisotropy
H. Vinnik et al. (2003)	Arabian Plate Lat 21–26 Lon 42–48	Ps and Sp, CSS, time	Saudi Arabian Broadband Array (8) ~18 months	350–410[c]	Dry mantle root — underlying wet mantle layer.
I. Saul et al. (2000)	Indian Shield Lat 17.4 Lon 78.6	Ps, CSS, freq.	perm. sta. HYB, 8 years	90[c]	Anisotropy
16. Kumar et al. (2007)[a]	Indian Ocean, surrounding area Lat −78 to 38 Lon 10–149	Sp, CSS, time	sta. (35)	200–300[a] S. Africa 101[a] India 90[a] S.E. Australia 164[a] S.W. Australia 180[a] N. Australia 80[a] Indian Ocean islands 257–293[a] S. Africa 187[a] central Africa 123[a] Tanzania 138[a] Arabian peninsula	
17. Wittlinger and Farra (2007)[c]	S. Africa Lat −35 to −17 Lon 14–32	Ps and Sp, CCP, time	array SASE (82) 1.5 – 2 years; Kimberly Array; perm. stas. SUR, BOSA, LBTB, LSZ	300[c]	Top of basaltic reservoir or ceiling of dense molten silicates from 410
18. Hansen et al. (2009)[c]	S. Africa Lat −30.5 to −26.5 Lon 23–29.5	Sp. CCP, time	array SASE (20) 1.5–2 years; AfricaArray (8) 1.5–2 years; perm. sta. BOSA	160[c]	
J. Savage and Silver (2008)	S. Africa Lat −33 to −19 Lon 18–32	Ps and Sp, stacks of entire array, and north vs. south, time and freq.	array SASE (82) 1.5–2 years	150[c]	Melt/metosomatic infiltration 4.5% drop over <10 km
K. Vinnik and Farra (2002)	S. Africa Lat −28.6 to −25.0 Lon 25.25 to −25.6	Sp, CSS, time	perm. stas. LBTB, BOSA, ~6 years	360[c] BOSA 280–300[c] LBTB	Related to continental flood basalts
19. Sodoudi et al. (2009)[c]	Central Alborz Lat 34–37 Lon 49–53	Sp[d], CSS, time	TTSN (11) 7 years	90[c]	
20. Kumar et al. (2005b)[b]	Tien Shan Lat 32.5–45 Lon 70–80	Sp, CCP, time	GHENGIS (28) <2 years; NANGA (6) 1–2 years; KNET (10); stas. KKAR, PDG, TLG, WUS, AAK, NIL	90–120[c] Tien Shan 160[c] Tarim Basin 270[c] Pamir and Karakoram orogenic belt (Asian lith) 130–170[c] Karakoram (Indian lith)	
21. Oreshin et al. (2002)[c]	Tien Shan Lat 39.5–44.5 Lon 73.75–80.25	Sp, CSS, time	KNET (9) ~10 years; GHENGIS (24) <2 years; stas. WUS, AAK, TLG, ~10 years	90[c]	6.7–8.9% assumed step function
22. Kumar et al. (2006)[b]	Himalayas Lat 27–36 Lon 86–100	Sp, CCP, time	Tibet exper., 1–2 years; INDEPTH II and III, 1–2 years; perm. sta. LSA	160[c] Himalayas, 220[c] S. of Bangong suture 160–180[c] Asian lith. central to northern Tibet	

Table 1 (continued)

Reference	Region	Method	Data	Depth summary (km)	Modeling and/or interpretation
	Approximate latitude	Data, stacking, domain	station or array (# stations)[e] running time[e]		
	Approximate longitude				
23. Sodoudi et al. (2006a)[b]	Dabie Shan in central eastern China Lat 29.25–34.5 Lon 114.5–117	Sp, CCP, time	temp. array (34) ~1 year	72[c] Yangtze 60[c] Sino-Korean	
24. Chen et al. (2006)[c]	Tanlu Fault Zone China Lat 36–37 Lon 117–120	Ps, CCP, time	NCISP-I (62) ~1 year	60–80[c]	3–7% over <10 km, composition or melt
25. Chen et al. (2008)[b]	N.E. North China Craton and Tanlu Lat 35–46 Lon 111–122	Sp, CCP, time	NCISP-I (62) ~1 year; NCISP-III (51) ~1.5 years; CEA (46) ~2 years	60–70[c] Tanlu 80–140[b] N.E. North China Craton	
26. Chen (2009)[c]	North China Craton Lat 36.5–40.5 Lon 112–120	Sp[d], CCP, time	NCISP-II (51)	80[c] Bohai Bay Basin 120[c] Taihang Mountains 90[c] North China Craton	
27. Kawakatsu et al. (2009)[c]	Philippine Sea Plate, WP1 Lat 18–20 Pacific Plate, WP2 Lat ~41 Lon ~160	Sp and Ps, CSS, time	borehole stas. WP1, WP2, a few years	76[c] beneath WP1 55[c] southeast of WP1 80[c] Pacific Plate	7–8% drop over less than 0–15 km

CSS = consider stations separately.

CCP = common conversion point.

[a] Values from a chart.

[b] Values inferred from a figure.

[c] Values from text of the paper.

[d] Study uses Ps and Sp, but consider Sp for the lithosphere–asthenosphere boundary estimate.

[e] if given.

[f] array data was considered as a single station due to close station spacing. perm. sta. stands for permanent station.temp. sta. stands for temporary station.

However, some shallow discontinuities interpreted as the lithosphere–asthenosphere boundary are located on Precambrian shields and platforms, including measurements on the Dharwar Craton (Kumar et al., 2007), northeastern Brazil (Heit et al., 2007), and the Arabian Peninsula (Hansen et al., 2007).

Ps and Sp image deeper discontinuities (150–300 km depth) also interpreted as the lithosphere–asthenosphere boundary, generally beneath continental interiors, for instance beneath the Slave Craton (190–220 km) (Snyder, 2008), the Tarim Basin (160 km), the Pamir and Karakoram orogenic belt (270 km) (Kumar et al., 2005b), central Brazil (160 km) (Heit et al., 2007), the Himalayas (160 km), south of the Bangong suture (220 km), Asian lithosphere from central Tibet to northern Tibet (160–180) (Kumar et al., 2006), the Kalahari Craton (~160–300 km) (Kumar et al., 2007; Wittlinger and Farra, 2007; Hansen et al., 2009), and the Arabian Platform (160 km) (Mohsen et al., 2006; Hansen et al., 2007). Many of these deeper discontinuities are imaged on or near Precambrian shields and platforms (Jordan, 1981), including the Slave Craton in Canada, central Brazil, Australia, Africa, and the Arabian Shield. However, some very deep results are nowhere near Precambrian environments, but rather beneath tectonically active regions such as the Himalayas, the Aegean subduction zone, the Tarim Basin, and the Pamir and Karakoram orogenic belt.

Many boundaries imaged near continental interiors dip toward the interior of the continents (Bostock, 1998; Kumar et al., 2005b; Kumar et al., 2006; Mercier et al., 2008; Snyder, 2008). Some have been interpreted as the base of the lithosphere (Kumar et al., 2005b; Kumar et al., 2006). Some are thought to be mid-lithospheric anisotropic boundaries that may be related to the formation of the continents (Bostock, 1998; Mercier et al., 2008). Overall, continental interiors are relatively complex (Levander et al., 2006).

5. Global comparison of receiver function results

Here we compare and contrast global receiver function results interpreted as the lithosphere–asthenosphere boundary. We present a global compilation in Fig. 1 as well as a summary of the results and the way they were obtained in Table 1. Though studies vary in terms of data processing and presentation, we have attempted to integrate them in a consistent fashion. If depths are reported in a table in a given publication, the table is used directly as input to Fig. 1. These cases usually correspond to single-station results, and therefore each station counts as a single data point. If depths are not reported in table format, then we attempt to translate depths reported in the text and figures of the publication into a similar format. For studies in which depths are reported in common conversion point bins, this could mean using a single value for each common conversion area shown in a results map. In situations where a single value is reported for a region where multiple stations are considered, we report the result(s) at the conversion point locations, if provided, or at locations that best represent the study region given the distribution of stations. Results are then simply smoothed over a 1.5-degree grid, which covers much of the width of Fresnel zones and the lateral distance between the station and the conversion point. In this scheme there is some degree of dependence on the format of presentation in the original publication, but we have attempted to represent studies in the most equitable way, minimizing our own influence, and noting that our focus is on identifying locations with discrepant results, and a global summary, rather than an average of proximal studies.

Putting an exact bound on when and where discrepancies exist is complicated by several factors already mentioned in the discussion of the synthesis of studies for Fig. 1. The data included, methodology (smoothing and/or filtering), conversion point locations, dips on a boundary, and the models used to migrate deconvolved waveforms to depth could all cause discrepant depths among studies. Migration model effects are relatively small, probably less than 5–10 km based on typical variations in crustal Vp/Vs, crustal depth, and mantle Vp/Vs, although they could be larger in situations with very deep discontinuities and anomalous Vp/Vs. The rest of the factors together can only explain discrepancies up to a certain point. For example, Sp hits the critical angle for conversion for events from back-azimuths in
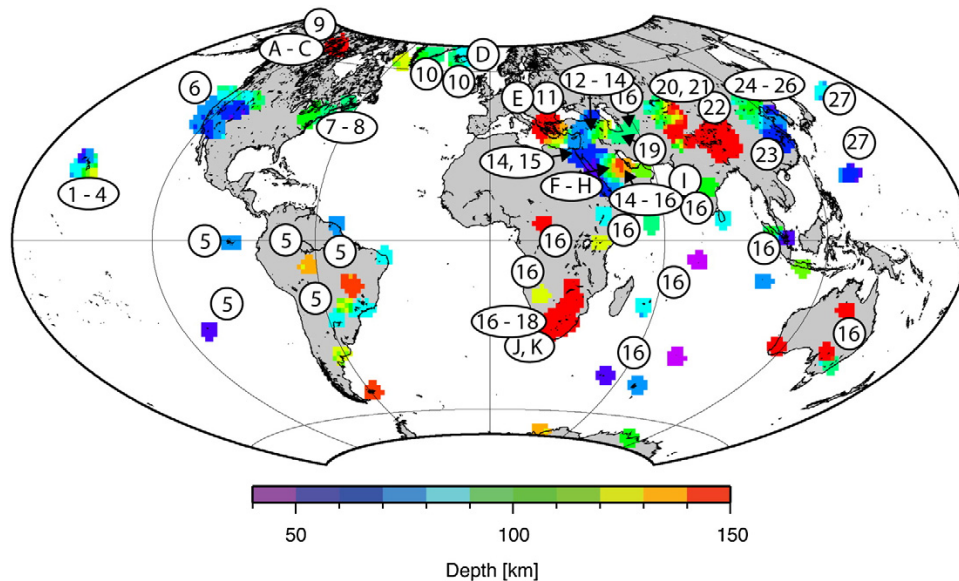
Fig. 1. Compilation of previous studies. Numbers correspond to the results listed in Table 1, and represent lithosphere–asthenosphere boundary interpretations. The background color corresponds to the depths reported by the nearest numbered studies. Lettered results represent studies that found velocity decreases with depth or changes in anisotropic orientation that were not necessarily termed the lithosphere–asthenosphere boundary. Lettered results are not included in the colored background, though their locations are indicated by the nearest colored regions since they are generally nearby other results, except for the case of E in which the study region is not colored. In some locations where multiple studies are in close proximity arrows connect labels with corresponding study regions.

the hemisphere opposite the dip direction when dip reaches angles of 10–25°, depending on the epicentral distance of the event. The Fresnel zone at 100 km depth is ~50–130 km for P waves and ~100–200 km for S waves. Given dip limits and Fresnel zone sensitivity widths, results within a degree of each other that differ by 20 km or more may be imaging different features, and results that differ by 50 km or more are likely discrepant. Of course, this is a generalization that is not valid for specific event distributions or irregular dips, and it is only valid for Sp. But it is a good starting point, given that the majority of studies discussed here use Sp waveforms (Table 1). We will consider waveform sensitivity in greater detail in a later section. Now we will continue by considering overlapping studies, those within a degree of each other, in two groups, those with large differences (>50 km), and those with more moderate differences (20–50 km).

Note that three studies would be in conflict if compared to themselves using the 50 km criteria above (Kumar et al., 2005b; Angus et al., 2006; Sodoudi et al., 2006a), but rapid variations might be expected in these locations given the tectonic environments, i.e., subducting and colliding lithosphere. In one case, variations are interpreted as multiple discontinuities, and a mélange of several lithospheric fragments (Angus et al., 2006). In another case a sloping boundary seems reasonable since the conversion point distribution is dominated by back-azimuths where an Sp conversion would be predicted (Sodoudi et al., 2006a). Although dipping boundaries may not produce an Sp converted phase from some back-azimuths, there is still the possibility of conversions from the other direction. We ignore instances where conflict is possible but not definite. For example, the work of Oreshin et al. (2002) reports a single depth for the Tien Shan region of ~90 km, whereas the work of Kumar et al. (2005b) presents spatially averaged bins. Overall, these results are in agreement within the Tien Shan as pointed out by Kumar et al. (2005b). However, just outside this region, beneath the Tarim Basin the Kumar et al. (2005b) result from bin 26 is quite deep >200 km. Broad interpretation of the work of Oreshin et al. (2002) could include this region given station locations. However, since piercing points are not reported in the work

of Oreshin et al. (2002), we cannot establish definitive conflict, and we assume agreement.

Regions where multiple local or regional receiver function studies have reported depths to a negative velocity discontinuity interpreted as the lithosphere–asthenosphere boundary include eastern North American, eastern China, Tien Shan, the Arabian Shield, eastern Turkey, Hawaii, and southern Africa. Of these, the regions of agreement, i.e., depths within 20 km, are eastern North America, eastern China, and Tien Shan. Ps depths agree with Sp depths beneath eastern North America and eastern China (Rychert et al., 2005; Chen et al., 2006; Rychert et al., 2007; Chen et al., 2008; Chen, 2009). Beneath Tien Shan Sp depths from two different studies are also in general agreement (Oreshin et al., 2002; Kumar et al., 2005b).

Beneath the Arabian Peninsula and Hawaii there is moderate disagreement among studies. On the Arabian Peninsula an Sp result for a single station (RAYN) (Kumar et al., 2007) is 22–24 km shallower than the Sp results of two other studies (Mohsen et al., 2006; Hansen et al., 2007). Beneath the eastern Anatolian Accretionary Complex an Sp study (Mohsen et al., 2006) finds depths 23–30 km deeper than those of both a Ps and an Sp study (Angus et al., 2006; Ozacar et al., 2008). Beneath Hawaii Ps depths (Li et al., 2000) are ~30 km deeper than those using Sp (Li et al., 2004) and 25–40 km deeper than another Ps study that utilized a larger array (Wolbern et al., 2006). Although the results are not technically overlapping, another example of studies at the edge of moderate disagreement is eastern China where Sp depths beneath the Sino-Korean Craton (Sodoudi et al., 2006b) are ~25 km shallower than Sp depths about a degree away to the northeast (Chen et al., 2008).

The one location with large depth discrepancies (>50 km) among lithosphere–asthenosphere boundary depths is southern Africa. Sp depths that considered two permanent stations (Kumar et al., 2007) reported depths of 257 and 293 km. A study that used both Sp and Ps from two seismic arrays, the same permanent stations and two other permanent stations reported a lithosphere–asthenosphere boundary at 300 km depth (Wittlinger and Farra, 2007). However, another Sp

study using arrays and one of the permanent stations reported a much shallower lithosphere–asthenosphere boundary at 160 km depth (Hansen et al., 2009). Another array study considering both Ps and Sp waveforms reported a discontinuity at 150 km depth, but interpreted it as a mid-lithospheric discontinuity related to melt/metasomatic infiltration (Savage and Silver, 2008).

Globally, there is general agreement among receiver function studies regarding the depth to boundaries interpreted as the lithosphere–asthenosphere boundary among regional spatially overlapping studies that consider either Ps or Sp. These studies report thick lithosphere (150–300 km) beneath or nearby Precambrian shields and platforms, but also beneath some orogenic zones, and thin lithosphere (40–120) beneath oceans and Phanerozoic magmatic/orogenic zones, but also beneath some Phanerozoic platforms and Precambrian shields and platforms. Moderate discrepancies exist in a few regions; however, beneath southern Africa discrepancies are larger and more difficult to reconcile.

6. Comparison with a global Ps study

The global Ps study of Rychert and Shearer (2009) is not included in Fig. 1 as it may not represent the lithosphere–asthenosphere boundary in all locations. To further investigate this question, we compare the previous lithosphere–asthenosphere boundary compilation presented in Fig. 1 with the recent Ps global study by combining them in Fig. 2. When the global Ps results are included there is much more global overlap, and even more locations of agreement including Hawaii, Easter Island, eastern and western North America, South America, Tanzania, the Arabian Peninsula, Tien Shan, southeastern Australia, India, Greenland, and ocean islands around the Indian ocean (Rychert and Shearer, 2009).

However, when the new Ps global study is included, conflicts also exist in several locations, and these regions are shown in black in Fig. 2, assuming the 50 km depth differential criteria. All conflicts are with previous studies that used Sp waveforms, and in all cases the Ps depth is shallower than that of Sp. Beneath central and southern Africa Ps is shallower than Sp by ~64–200 km depending on which study is considered (Kumar et al., 2007; Wittlinger and Farra, 2007; Hansen et al., 2009). Beneath northern and southwestern Australia, Ps is shallower by ~75 and ~90 km respectively, although the global Ps

study also found a weak arrival at depths consistent with the Sp result from the southwest (Kumar et al., 2007). Ps depths are shallower by 100–125 km beneath southern Europe (Sodoudi et al., 2006a), 65–90 km beneath the Tamir Basin, south of Tien Shan (Kumar et al., 2005b), and ~50 km beneath the Arabian Peninsula (Mohsen et al., 2006; Hansen et al., 2007).

Smaller discrepancies (20–50 km) between the Rychert and Shearer (2009) Ps result and previous studies include western North America (Ps deeper by ~30 km in some cases) (Li et al., 2007), Tanzania (Ps shallower by ~25 km) (Kumar et al., 2007), Brazil (Ps shallower by ~30–50 km) (Heit et al., 2007), Easter Island (Ps deeper by ~30 km), one of the islands in the Indian Ocean (Ps shallower by ~25 km) (Kumar et al., 2007), Hawaii (Ps deeper than Sp by ~30 km (Li et al., 2004) and one Ps study (Wolbern et al., 2006) but in agreement with another Ps study (Li et al., 2000)), one result from the North Atlantic (Ps shallower than Sp by ~30 km) (Kumar et al., 2005a), and the eastern Anatolian Accretionary Complex (Ps global result ~30–40 km deeper than both a Ps and an Sp study (Angus et al., 2006; Ozacar et al., 2008) but in agreement with another Sp study (Mohsen et al., 2006)).

Ps–Sp discrepancies are not surprising in that they can be explained by a variety of scenarios. Multiple boundaries could exist, each being detected or interpreted by only one study. Boundaries could be anisotropic, occur over different depth ranges, and/or vary laterally in strength or depth. All of these factors will create different receiver function results depending on the distribution of events and stations, the type of receiver function (Ps or Sp), and the processing used. In fact, multiple boundaries are relatively common (Rychert et al., 2005; Li et al., 2007; Rychert et al., 2007). They are frequently observed beneath orogenic/magmatic zones (Rychert and Shearer, 2009) but also beneath cratonic environments (Bostock, 1998). Additional velocity decreases with depth have been reported beneath regions that we have previously discussed, though not necessarily interpreted as the lithosphere–asthenosphere boundary, for instance both shallower and deeper beneath southern Africa (Vinnik and Farra, 2002; Savage and Silver, 2008), deeper beneath the Arabian Peninsula (Vinnik et al., 2003), and shallower beneath the Slave Craton (Yuan et al., 2006). Boundaries in anisotropy without a lithosphere–asthenosphere boundary designation have also been reported beneath the Slave Craton (layering at 70–80 km
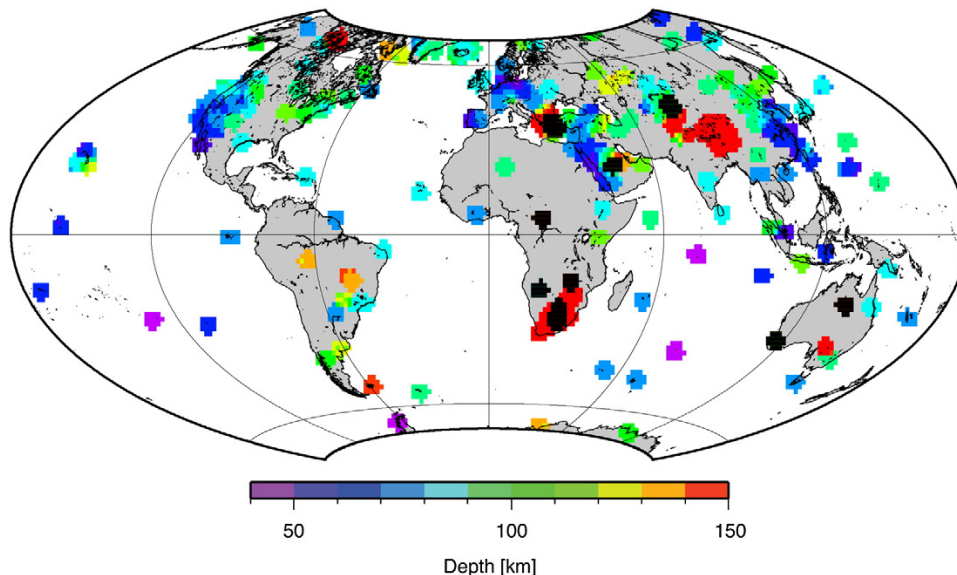

Fig. 2. Compilation of previous studies, including a recent global Ps study (Rychert and Shearer, 2009). The colors represent the depth of the lithosphere–asthenosphere boundary from the numbered studies in Fig. 1 as well as the global Ps study. Black regions are those in which Ps global results disagree with previous results, i.e., results that are less than 1° apart with depths that are different by 50 km or more.

and 120–150 km and a boundary dipping from 170 to 230 km) (Bostock, 1998), the southwest German basin (Farra and Vinnik, 2000), the Dharwar Craton (90 km) (Saul et al., 2000), the eastern edge of the Arabian Shield (70 km) (Levin and Park, 2000), and northwestern Canada (dipping 30 to 90 km) (Mercier et al., 2008). Beneath cratons shallow sharp boundaries may represent fossil fabric from slab structures originally stacked in the formation of the continents.

7. Modeling

Modeling the velocity gradients associated with imaged boundaries is an important way to better understand discrepancies, and constrain the mechanisms responsible for the observed discontinuities. Some studies have modeled converted phases to constrain gradient parameters. Examples include eastern North America (5–10% velocity drop over 11 km or less) (Rychert et al., 2005, 2007), the Tanlu fault zone China (3–7% drop over <10 km) (Chen et al., 2006), Hawaii (a step-function-like 10–20% drop) (Li et al., 2000; Collins et al., 2002), and the Philippine Plate (7–8% drop in velocity over less than 10–15 km depth) (Kawakatsu et al., 2009). Overall, when the velocity gradients are modeled, as described above, they are strong and sharp. Thermal gradients alone are too gradual to define such contrasts, and other mechanisms are required. In some cases, a velocity drop is constrained, but the depth range over which it occurs is not necessarily modeled, and a step function is assumed, e.g., (Oreshin et al., 2002), and in many cases modeling is not performed (Table 1). However, we can make some inferences regarding the meaning of global results in the absence of detailed modeling.

8. Waveform sensitivity

Both Ps and Sp phases are generated at boundaries that are sharp. For example, two step-function velocity drops will be seen as distinct phases until their separation distance is less than approximately wavelength/2 (Bostock and Rondenay, 1999; Rychert et al., 2007). This distance is greater for Sp than it is for Ps, i.e., roughly ~5–20 km for Ps and ~15–30 km for Sp in the depth range of the lithosphere–asthenosphere boundary. The difference is caused by the inherently longer dominant period of the Sp phase.

Fig. 3 demonstrates sensitivity of Ps and Sp waveforms for a range of gradients and dominant periods. The model assumes a 6% velocity drop in depth in both P and S wave velocity. Vs in the upper layer is 4.556 km/s and Vp/Vs and density in both layers are fixed at 1.8 and 3.32 g/cm³, respectively. Amplitudes of waveforms that are converted at linear velocity gradients are compared to the amplitudes of converted phases generated at sharp, step-function velocity drops. The comparison is done on the raw waveform, i.e. before deconvolution. Results are reported in terms of the incident wavelength as well as the average wavelength across the velocity gradient.

The main difference in sensitivity of Ps and Sp waveforms in Fig. 3 is that the wavelengths of Sp phases are generally longer than those of Ps. Therefore, although Ps and Sp are both produced at very sharp velocity gradients, Sp conversions are also produced at velocity gradients too gradual to produce a Ps phase.

Fig. 4 explores the possibility that Ps and Sp phases originate from a thermal gradient in the mantle. The black (Ps) and grey (Sp) lines in the figure demonstrate the velocity drops at gradational boundaries required to match the amplitudes of converted phases that are generated at sharp, step-function velocity drops of 2% and 5% for fixed representative dominant periods (1 and 4 s for Ps and 7 and 14 s for Sp). These lines were calculated by considering the amplitudes of converted phases in a number of synthetic seismograms. A thick velocity gradient must also have a large velocity contrast if it is to produce a converted phase that is similar in amplitude to one created at a step-function velocity discontinuity. The colored lines were calculated by scaling shear velocity in the lithosphere and the asthenosphere to temperature assuming the relationships and parameters of Faul and Jackson (2005), two different
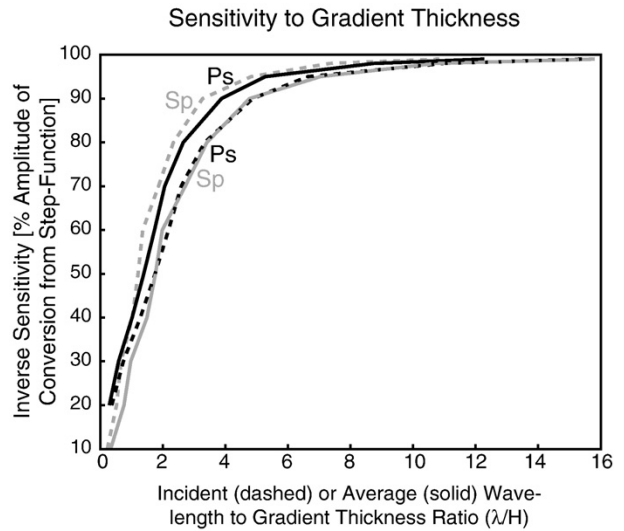

Fig. 3. Sensitivity of Ps and Sp to velocity gradient thickness. The amplitudes of converted Ps (black lines) and Sp (grey lines) phases from velocity gradients of various thicknesses are compared to those from single step-function velocity drops of the same magnitude. We consider the amplitudes of synthetic seismograms on the transformed S component for Ps conversions and the transformed P component for Sp conversions. Since sensitivity is dependent on the dominant period of the incident waveform, we have also varied this parameter. Sensitivity to a given gradient can then be described as the percent amplitude of a converted phase from a step-function velocity drop exhibited by a conversion with a given incident (dashed line) or average (solid lines) wavelength-to-gradient thickness ratio. Our model assumes a 6% velocity drop in P and S wave velocity, S wave velocity in the upper layer of 4.556, density of 3.32 g/cm³ and Vp/Vs = 1.8. The slownesses are set at representative values of 6.34 and 12.12 s/degree for Ps and Sp, respectively. Note that a plotting error in the average wavelength-to-gradient thickness ratio in the previously published version of this figure in the work of Rychert et al. (2007) has been corrected here.
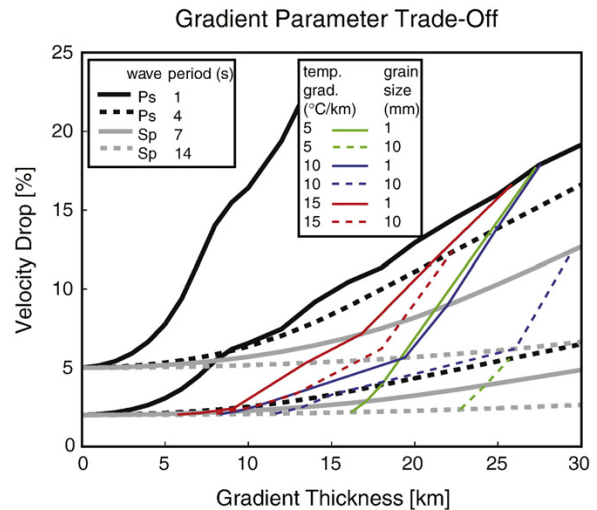

Fig. 4. Gradients responsible for converted phases compared to those expected from thermal contours. Black and grey lines represent the magnitude of the velocity gradient required to maintain amplitude of a converted phase created at a step-function discontinuity with increasingly gradual gradients. This is demonstrated for reference velocity drops of 2% and 5% at zero gradient thickness. Periods are representative of Ps: 1 s (black solid lines) and 4 s (black dashed lines), and Sp: 7 s (grey solid lines) and 14 s (grey dashed lines). Colored lines representing 5 °C/km (green), 10 °C/km (blue), and 15 °C/km (red) thermal gradients are shown for grain sizes of 1 mm (solid) and 1 cm (dashed) assuming the parameters and relationships of Faul and Jackson (2005).

grain sizes (1 and 10 mm), and representative Ps and Sp dominant periods. Interpolation was used to connect points with the same thermal gradient: 5 (green), 10 (blue), and 15 °C/km (red). Gradients to the right of the colored lines could be thermally defined, while those to the left cannot be defined by temperature alone.

Determining the thermal gradient that may define a seismic conversion depends somewhat on the parameters of the upper mantle, i.e., grain size, activation energy, and thermal gradients. The relationships of Faul and Jackson (2005) allow us to make some predictions for the expected effects of temperature on velocity, and numerical experiments provide some constraint on the thermal gradients in the mantle. Thermal gradients at the lithosphere–asthenosphere boundary are probably not more than 10 °C/km. Numerical modeling in which viscosity is dependent on pressure and temperature find thermal gradients that are typically no greater than 10 °C/km at the lithosphere–asthenosphere boundary, and gradients are less than ~15 °C/km throughout the entire lithosphere (King and Ritsema, 2000; Zaranek et al., 2005).

The velocity drop required for Ps phases from velocity gradients that are gradual is large, and gradients that may explain observed Ps phases are generally sharper than those expected from thermal gradients alone, i.e. on the left-hand side of the blue 10 °C/km contour in Fig. 4. However, a long period Sp phase (~14 s) created at a 5% velocity drop that occurs as a step function will have approximately the same amplitude as a phase from a drop that occurs over depths of ~20 or ~25 km, i.e., approaching the zone that may be defined by thermal gradients. In other words, amplitudes for the long period Sp phase (dashed grey line in Fig. 4) are about the same on either side of the 10 °C/km contours (blue lines in Fig. 4). Therefore, while constraints from individual studies on the dominant period of the Sp waveform may be able to preclude thermal gradients in some cases, Sp phases may also originate from thermal boundaries. Given the trade-off in gradient parameters for Ps, thermal origins are far less likely.

9. Mechanisms that may explain sharp boundaries

What mechanism can explain the sharp boundaries imaged by Ps? Other mechanisms besides temperature that affect seismic velocities include composition, partial melting, anisotropy, and grain size.

It has been proposed that the continental lithosphere is depleted in elements such as iron in comparison to the underlying asthenosphere. A boundary in depletion can explain a velocity drop of up to 0.9–2.3% (Lee, 2003; Schutt and Lesher, 2006). The lower end of this estimate comes from lab sample compositions (Schutt and Lesher, 2006) while the upper end comes from natural continental compositions (Lee, 2003). A boundary in composition could be sharp enough to explain Ps converted phases. However, the magnitude of the expected velocity drop is probably insufficient, at least by itself, to explain most observations.

It has also been proposed that the lithosphere is dehydrated in comparison to the asthenosphere. Assuming that hydration affects seismic velocities via attenuation (Karato, 2003), global attenuation values (Dalton et al., 2008), and the relationships of Faul and Jackson (2005), a dehydration boundary at ~100 km depth may explain seismic velocity drops of ~4.5% beneath continents and up to ~5.7% beneath oceans. These estimates are bounded by global attenuation values beneath the stations used in the work of Rychert and Shearer (2009), assuming typical Ps dominant periods (1–5 s), a grain size of 1 mm and the parameter values in the work of Faul and Jackson (2005). Since global attenuation results may average local structure, these bounds could be expanded slightly, though the minimum global Q (inverse attenuation) values used to make these calculations are already quite low, $Q = 46$ and 48 beneath oceans and Phanerozoic magmatic/orogenic zones and $Q = 100$ and 70 beneath Phanerozoic platforms and Precambrian shields and platforms. In other words, without considering the frequency dependence of attenuation some of these Q values are lower than some of those found in subduction zone wedges using higher frequency waveforms, where hydration is thought to cause very high attenuation (Rychert et al., 2008). The Q values above are for periods of 75 s and would be even smaller at 1 Hz, where many regional studies report Q, given the frequency dependence of attenuation.

Alternatively, a small amount of partial melting in the asthenosphere (Anderson, 1989; Mierdel et al., 2007) could easily produce a strong, sharp boundary (Rychert et al., 2007; Kawakatsu et al., 2009). The levels of melting required to explain the magnitudes of the modeled velocity contrasts are on the order of 1–5 wt.% (Hammond and Humphreys, 2000; Takei, 2002; Kreutzmann et al., 2004; Rychert et al., 2007; Kawakatsu et al., 2009). Whether or not this amount of melting exists in the mantle locally or globally is debated. Decompression melting could occur as mildly hydrated asthenosphere moves along the edge of continental keels (Rychert et al., 2007). Alternatively, melt could exist without the need for decompression melting (Anderson, 1989), perhaps in bands (Holtzman et al., 2003; Kawakatsu et al., 2009; Takei and Holtzman, 2009). It has been suggested that variation in water solubility, i.e., a sharp increase in aluminous orthopyroxene and a more gradual increase in olivine with depth may enable melting in the asthenosphere (Mierdel et al., 2007).

Finally, a decrease in radial anisotropy with depth can cause a converted wave with the same polarity as one from a velocity decrease with depth. This kind of mechanism could be frozen-in within cratonic structures, and caused by some unknown process in the past. However, it is not likely that this type of mechanism by itself can explain observations beneath continental margins or oceans, since a mechanism to create the sharp transition in anisotropy, such as hydration, would probably still be required. The same is true in the case of azimuthal anisotropy and also grain size. In addition, in the case of azimuthal anisotropy, back-azimuthal variation in amplitude should be detectable. A boundary that is purely defined by azimuthal anisotropy could be visible in a single stack, especially if the signal is dominated by events from a single back-azimuth.

10. Is it the lithosphere–asthenosphere boundary?

Determining whether boundaries imaged by receiver functions represent mid-lithospheric features or the base of the rigid lid can be challenging. In some regional studies, clear agreement has been shown between the gradual drop in velocity from regional surface-wave studies and receiver function depths (Kumar et al., 2005b; Rychert et al., 2005, 2007). In addition, tectonically averaged global receiver function results are within the gradual drop in velocity from global surface waves (Nettles and Dziewonski, 2008; Rychert and Shearer, 2009). However, this correlation does not stand beneath each individual station. In addition, global correlation between receiver function results and the mean or median depth of the gradual drop in velocity from global tomography has not been established. This could be because surface waves may be relatively insensitive to the exact depth of a sharp boundary. Surface waves can easily average more complicated fine-scale structure laterally or in depth, and thus comparisons can be challenging.

Shallow velocity decreases with depth imaged by Ps (65–134 km) (Rychert and Shearer, 2009) and Sp (86–120 km) (Yuan et al., 2006; Hansen et al., 2007; Heit et al., 2007; Kumar et al., 2007) have been reported at stations that are technically on Precambrian lithosphere in the tectonic realization that is based on surface features (Jordan, 1981). Some reported shallow discontinuities could be located at the edge of the craton, while others could be imaging mid-lithospheric discontinuities. In situations where Sp images deeper discontinuities than Ps (black regions in Fig. 2), Ps is likely imaging mid-lithospheric discontinuities. In the remainder of cases, distinguishing mid-lithospheric discontinuities from measurements that reflect the edges of cratons is more difficult. Fig. 5 illustrates the locations of the stations used by Rychert and Shearer (2009) in relationship to the

tectonic regionalization of Jordan (1981). Many stations located on Precambrian shields and platforms (green triangles) are near tectonic boundaries (the edges of the black surface). Furthermore, the exact location of the seismically fast cratonic lid at depth may not be directly correlated with the oldest surface realizations, for instance in Australia where the lithosphere is in places thicker beneath the central Proterozoic section than it is beneath the Archean lithosphere in the east (Simons et al., 1999; Fishwick et al., 2005; Fishwick et al., 2008). Regional results are better for comparison but do not exist in all locations, and global comparisons of these results are hampered by variations in array aperture and methodology.

The existence of shallow strong, sharp negative boundaries that extend over wide areas beneath cratons conflicts with global tomographic models in which cratons are seismically fast to 200–250 km depth, unless these drops in shear velocity do not correspond to mechanically weak zones. A common notion is that the craton is chemically distinct to ~175 km to satisfy constraints from xenoliths, with a deeper thermal root to satisfy the deeper signature from seismic tomography (King, 2005; Lee et al., 2005). If a sharp shallow pervasive boundary exists and corresponds to a drop in viscosity, it would necessarily cause decoupling of the lower layer, and the erosion of any thermal root. Alternatively, frozen-in anisotropic and/or compositional boundaries can be responsible for sharp, shallow discontinuities. These could be related to the creation of the craton, i.e., multiple slabs with various anisotropic orientations that have been stacked together (Bostock, 1998) or modification of existing cratonic lithosphere by melt transport and metasomatism (Savage and Silver, 2008).

Though Sp has imaged deep boundaries beneath cratonic interiors, deep cratonic discontinuities that are imaged using Ps alone are much more rare, though examples exist. For instance a boundary dipping from 190 to 220 km depth (Snyder, 2008), an anisotropic boundary dipping from 170 to 230 km depth, and an isotropic boundary at 350 km (Bostock, 1998) have been imaged beneath the Slave Craton, and a discontinuity at 350–410 km depth has been imaged beneath Arabia (Vinnik et al., 2003). One reason could be that interference from reverberations obscures deep boundaries. Alternatively, sharp contrasts like those more commonly imaged beneath oceans and margins may not exist at depth (~200–250 km) beneath cratons, i.e., depths consistent with the extent of anomalies from global and regional tomography. In this case cratons would be defined thermally at depth. However, it will be difficult to assert that sharp boundaries do not exist in certain locations. Reverberations will always obscure sections of Ps data and it is difficult to be sure of anything in locations where no clear Moho exists, i.e., the Moho boundary itself is weak, or locations where strong shallow sediment structure interfaces cause severe ringing. In addition, it may be difficult to assess the sharpness of discontinuities that are imaged by Sp alone. However, if sharpness can be constrained, problems regarding existence can still arise because Sp is generally noisy, individual Sp conversion points can be separated by large lateral distances, and its long period nature can cause phases to be very close together, raising questions regarding whether they represent real structure or side lobes of other phases. One way to better understand Earth structure is to consider both Ps and Sp at different frequencies with both time and frequency domain methods (e.g. Savage and Silver, 2008; Abt et al., 2010).

Agreement between Ps and Sp provides the most definitive results since the two phases give independent confirmation that the discontinuity exists (Rychert et al., 2007). However, since the phases have different sensitivities owing to variations in conversion point and dominant period, consideration of the two may not necessarily give the simplest answers, and it may reveal even greater complexity. Similarly, anisotropic origins should be considered in greater detail globally, although putting tight constraints on anisotropy using receiver functions can be difficult since good back-azimuthal distribution is dependent on source distribution, and also since the receiver functions are often lower quality owing to significantly reduced quantities of data in each bin. In most cases, more comprehensive and detailed imaging and modeling should help. High frequency results at single stations require at least 5, but preferably 10 years of data for a clear image. However, lateral resolution requires dense arrays that can track transitions between ocean and craton. In addition, better coverage of cratonic areas is required, where the boundary may be deep, or not very sharp, especially since a negative result (i.e., no sharp
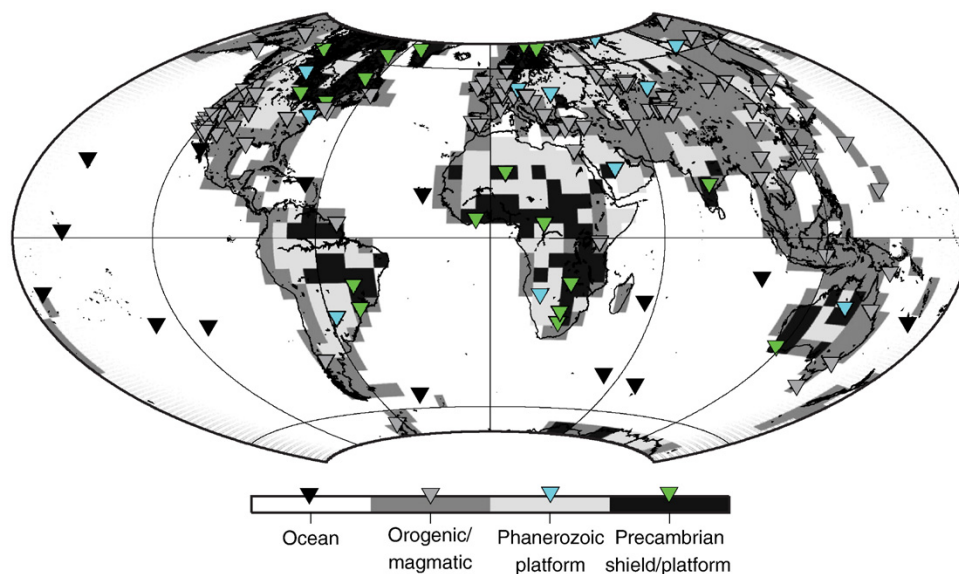

Fig. 5. Tectonic regionalization compared to station locations. Triangles show the 169 stations used by Rychert and Shearer (2009). Station color and background color correspond to tectonic regionalization, after Jordan (1981). Tectonic regions are colored as follows: oceanic — black triangles on white background, Phanerozoic orogenic zones and magmatic belts — dark grey triangles and background, Phanerozoic platforms — cyan triangles on light grey background, and Precambrian shields and platforms — green triangles no black background. Although the work of Jordan (1981) divides oceanic environments into three age groupings, a single oceanic bin, encompassing all ages, is used to group the seismic stations, since sampling of this region is sparse.

boundary exists) is much more difficult to assert than a positive one. A full understanding of lithospheric rheology and its relationship to the asthenosphere will require high-resolution global imaging integrated with other data sets such as tomography, electromagnetic, gravity, thermal, and chemical, combined with numerical modeling. Recent attempts to correlate surface-wave tomography with other geophysical observables such as crustal thickness, gravity, and heat flow are promising (Boschi et al., 2009; Fry et al., 2009).

Negative discontinuities have been identified beneath a wide range of tectonic environments. Results that image boundaries interpreted as the lithosphere–asthenosphere boundary are numerous. There is still debate over what exactly is being imaged, and evidence exists for multiple discontinuities in some regions. In addition, the abundance of positive results does not necessarily eliminate the possibility that some regions are characterized by gradual lithosphere–asthenosphere boundaries. However, if seismic imaging does eventually resolve a globally pervasive boundary that is strong and sharp, requiring a mechanism such as dehydration or melting to explain it, a fundamental boundary would necessarily be implied, i.e., the lithosphere–asthenosphere boundary.

Acknowledgements

References

Abt, D., Fischer, K., French, S., Ford, H., Yuan, H., 2010. North American lithospheric discontinuity structure imaged by Ps and Sp receiver functions. Journal of Geophysical Research—Solid Earth 115, B09301. doi:10.1029/2009JB006914.

Anderson, D.L., 1989. Theory of the Earth. Blackwell Sci, Boston, MA.

Angus, D.A., Wilcon, D.C., Sandvol, E., Ni, J.F., 2006. Lithospheric structure of the Arabian and Eurasian collision zone in eastern Turkey from S-wave receiver functions. Geophysical Journal International 166, 1335–1346. doi:10.1111/j.1365-246X.2006.03070.x.

Bagley, B., Revenaugh, J., 2008. Upper mantle seismic discontinuities of the Pacific. Journal of Geophysical Research—Solid Earth 113 (B12301). doi:10.1029/2008JB005692.

Boschi, L., Fry, B., Ekstrom, G., Giardini, D., 2009. The European upper mantle as seen by surface waves. Surveys in Geophysics 30 (4–5). doi:10.1007/s10712-009-9066-2.

Bostock, M.G., 1998. Mantle stratigraphy and evolution of the Slave province. Journal of Geophysical Research—Solid Earth 103 (B9), 21,183–21,200.

Bostock, M.G., 1999. Seismic imaging of lithospheric discontinuities and continental evolution. Lithos 48 (1–4), 1–16.

Bostock, M.G., Rondenay, S., 1999. Migration of scattered teleseismic body waves. Geophysical Journal International 139 (2), 597.

Chen, L., 2009. Lithospheric structure variations between the eastern and central North China Craton from S- and P-receiver function migration. Physics of the Earth and Planetary Interiors 173 (3–4), 216–227. doi:10.1016/j.pepi.2008.11.011.

Chen, L., Zheng, T.Y., Xu, W.W., 2006. A thinned lithospheric image of the Tanlu Fault Zone, eastern China: constructed from wave equation based receiver function migration. Journal of Geophysical Research—Solid Earth 111, B09312. doi:10.1029/2005JB003974.

Chen, L., Tao, W., Zhao, L., Zheng, T.Y., 2008. Distinct lateral variation of lithospheric thickness in the northeastern North China Craton. Earth and Planetary Science Letters 267 (1–2), 56–68.

Christensen, N.I., Mooney, W.D., 1995. Seismic velocity structure and composition of the continental crust: a global view. Journal of Geophysical Research—Solid Earth 100 (B7), 9761–9788.

Collins, J.A., Vernon, F.L., Orcutt, J.A., Stephen, R.A., 2002. Upper mantle structure beneath the Hawaiian swell: constraints from the ocean seismic network pilot experiment. Geophysical Research Letters 29 (11), 1522. doi:10.1029/2001GL013302.

Dalton, C.A., Ekstrom, G., Dziewonski, A.M., 2008. The global attenuation structure of the upper mantle. Journal of Geophysical Research—Solid Earth 113, B09303. doi:10.1029/2007JB005429.

Farra, V., Vinnik, L., 2000. Upper mantle stratification by P and S receiver functions. Geophysical Journal International 141 (3), 699–712.

Faul, U.H., Jackson, I., 2005. The seismological signature of temperature and grain size variations in the upper mantle. Earth and Planetary Science Letters 234 (1–2), 119–134.

Fishwick, S., Kennett, B.L.N., Reading, A.M., 2005. Contrasts in lithospheric structure within the Australian Craton — insights from surface wave tomography. Earth and Planetary Science Letters 231 (3–4), 163–176.

Fishwick, S., Heintz, M., Kennett, B.L.N., Reading, A.M., Yoshizawa, K., 2008. Steps in lithospheric thickness within eastern Australia, evidence from surface wave tomography. Tectonics 27 (4). doi:10.1029/2007TC002116.

Forsyth, D.W., 1985. Subsurface loading and estimates of the flexural rigidity of continental lithosphere. Journal of Geophysical Research—Solid Earth 90 (B14), 12,623–12,632.

Fry, B., Boschi, L., Ekstom, G., Giardini, D., 2009. Europe–Mediterranean tomography: high correlation between new seismic data and independent geophysical observables. Geophysical Research Letters 35 (L04301). doi:10.1029/2007GL031519.

Gaherty, J.B., Kato, M., Jordan, T.H., 1999. Seismological structure of the upper mantle: a regional comparison of seismic layering. Physics of the Earth and Planetary Interiors 110 (1–2), 21–41.

Gung, Y.C., Panning, M., Romanowicz, B., 2003. Global anisotropy and the thickness of continents. Nature 422 (6933), 707–711.

Hammond, W.C., Humphreys, E.D., 2000. Upper mantle seismic wave velocity: effects of realistic partial melt geometries. Journal of Geophysical Research—Solid Earth 105 (B5), 10,975–10,986.

Hansen, S.E., Rodgers, A.J., Schwartz, S.Y., Al-Amri, A.M.S., 2007. Imaging ruptured lithosphere beneath the Red Sea and Arabian Peninsula. Earth and Planetary Science Letters 259 (3–4), 256–265.

Hansen, S., Nyblade, A., Julia, J., Dirks, P., Durrheim, R., 2009. Upper-mantle low-velocity zone structure beneath the Kaapvaal craton from S-wave receiver functions. Geophysical Journal International 178, 1021–1027. doi:10.1111/j.1365-246X.2009.04178.x.

Harmon, N., Forsyth, D.W., Lamm, R., Webb, S.C., 2007. P and S wave delays beneath intraplate volcanic ridges and gravity lineations near the East Pacific Rise. Journal of Geophysical Research—Solid Earth 112 (B03309). doi:10.1029/2006JB004392.

Heit, B., Sodoudi, F., Yuan, X., Bianchi, M., Kind, R., 2007. An S receiver function analysis of the lithospheric structure in South America. Geophysical Research Letters 34 (L14307). doi:10.1029/2007GL030317.

Hirth, G., Evans, R.L., Chave, A.D., 2000. Comparison of continental and oceanic mantle electrical conductivity: is the Archean lithosphere dry? Geochemistry Geophysics Geosystems 1 (12), 1030. doi:10.1029/200GC00048.

Holtzman, B.K., Kohlstedt, D.L., Zimmerman, M.E., Heidelbach, F., Hiraga, T., et al., 2003. Melt segregation and strain partitioning: implications for seismic anisotropy and mantle flow. Science 301 (5637), 1227–1230.

Jordan, T.H., 1978. Composition and development of continental tectosphere. Nature 274 (5671), 544–548.

Jordan, T.H., 1981. Global tectonic regionalization for seismological data analysis. Bulletin of the Seismological Society of America 71 (4), 1131–1141.

Karato, S., 2003. Mapping water content in the upper mantle. In: Eiler, J. (Ed.), Inside the Subduction Factory. Geophys. Monogr. Ser. AGU, Washington, D. C., pp. 135–152.

Kawakatsu, H., Kumar, P., Takei, Y., Shinohara, M., Kanazawa, T., et al., 2009. Seismic evidence for sharp lithosphere–asthenosphere boundaries of oceanic plates. Science 324 (5926), 499–502. doi:10.1126/science.1169499.

King, S.D., 2005. Archean cratons and mantle dynamics. Earth and Planetary Science Letters 234 (1–2), 1–14.

King, S.D., Ritsema, J., 2000. African hot spot volcanism: small-scale convection in the upper mantle beneath cratons. Science 290 (5494), 1137–1140.

Kobussen, A.F., Griffin, W.L., O'Reilly, S.Y., Shee, S.R., 2008. Ghosts of lithospheres past: imaging an evolving lithospheric mantle in southern Africa. Geology 36 (7), 515–518.

Kreutzmann, A., Schmeling, H., Junge, A., Ruedas, T., Marquart, G., et al., 2004. Temperature and melting of a ridge-centred plume with application to Iceland. Part II: predictions for electromagnetic and seismic observables. Geophysical Journal International 159 (3), 1097–1111.

Kumar, P., Kind, R., Hanka, W., Wylegalla, K., Reigber, C., et al., 2005a. The lithosphere–asthenosphere boundary in the North–West Atlantic region. Earth and Planetary Science Letters 236 (1–2), 249–257.

Kumar, P., Yuan, X., Kind, R., Kosarev, G., 2005b. The lithosphere–asthenosphere boundary in the Tien Shan–Karakoram region from S receiver functions: evidence for continental subduction. Geophysical Research Letters 32 (7), L07305. doi:10.1029/2004GL022291.

Kumar, P., Yuan, X.H., Kind, R., Ni, J., 2006. Imaging the colliding Indian and Asian lithospheric plates beneath Tibet. Journal of Geophysical Research—Solid Earth 111 (B6), B06308. doi:10.1029/2005JB003930.

Kumar, P., Yuan, X.H., Kumar, M.R., Kind, R., Li, X.Q., et al., 2007. The rapid drift of the Indian tectonic plate. Nature 449 (7164), 894–897.

Kustowski, B., Ekstrom, G., Dziewonski, A.M., 2008. Anisotropic shear-wave velocity structure of the Earth's mantle: a global model. Journal of Geophysical Research—Solid Earth 113 (B6), B06306. doi:10.1029/2007JB005169.

Lebedev, S., van der Hilst, R.D., 2008. Global upper-mantle tomography with the automated multimode inversion of surface and S-wave forms. Geophysical Journal International 173 (2), 505–518.

Lee, C.T.A., 2003. Compositional variation of density and seismic velocities in natural peridotites at STP conditions: implications for seismic imaging of compositional heterogeneities in the upper mantle. Journal of Geophysical Research—Solid Earth 108 (B9), 2441. doi:10.1029/2003JB002413.

Lee, C.T.A., Lenardic, A., Cooper, C.M., Niu, F.L., Levander, A., 2005. The role of chemical boundary layers in regulating the thickness of continental and oceanic thermal boundary layers. Earth and Planetary Science Letters 230 (3–4), 379–395.

Levander, A., Niu, F.L., Lee, C.T.A., Cheng, X., 2006. Imag(in)ing the continental lithosphere. Tectonophysics 416 (1–4), 167–185.

Levin, V., Park, J., 2000. Shear zones in the Proterozoic lithosphere of the Arabian Shield and the nature of the Hales discontinuity. Tectonophysics 323, 131–148.

Li, A., Burke, K., 2006. Upper mantle structure of southern Africa from Rayleigh wave tomography. Journal of Geophysical Research—Solid Earth 111 (B10), B10303. doi:10.1029/2006JB004321.

Li, X., Kind, R., Priestley, K., Sobolev, S.V., Tilmann, F., et al., 2000. Mapping the Hawaiian plume conduit with converted seismic waves. Nature 405 (6789), 938–941.

Li, A., Forsyth, D.W., Fischer, K.M., 2003. Shear velocity structure and azimuthal anisotropy beneath eastern North America from Rayleigh wave inversion. Journal of Geophysical Research—Solid Earth 108 (B8), 2362. doi:10.1029/2002JB002259.

Li, X., Kind, R., Yuan, X.H., Wolbern, I., Hanka, W., 2004. Rejuvenation of the lithosphere by the Hawaiian plume. Nature 427 (6977), 827–829.

Li, X., Yuan, X.H., Kind, R., 2007. The lithosphere–asthenosphere boundary beneath the western United States. Geophysical Journal International 170 (2), 700–710. doi:10.1111/j.1365-246X.2007.03428.x.

Ligorria, J., Ammon, C., 1999. Iterative deconvolution and receiver-function estimation. Bulletin of the Seismological Society of America 89, 1395–1400.

Marone, F., Gung, Y.C., Romanowicz, B., 2007. Three-dimensional radial anisotropic structure of the North American upper mantle from inversion of surface waveform data. Geophysical Journal International 171 (1), 206–222.

McKenzie, D., Fairhead, D., 1997. Estimates of the effective elastic thickness of the continental lithosphere from Bouger and free air gravity anomalies. Journal of Geophysical Research—Solid Earth 102 (B12), 27,523–27,552.

Mercier, J., Bostock, M., Audet, P., Gaherty, J., Garnero, E., et al., 2008. The teleseismic signature of fossil subduction: Northwestern Canada. Journal of Geophysical Research—Solid Earth 113 (B4). doi:10.1029/2007JB005127.

Mierdel, K., Keppler, H., Smyth, J.R., Langenhorst, F., 2007. Water solubility in aluminous orthopyroxene and the origin of Earth's asthenosphere. Science 315 (5810), 364–368.

Mohsen, A., Kind, R., Sobolev, S.V., Weber, M., Grp, D., 2006. Thickness of the lithosphere east of the Dead Sea Transform. Geophysical Journal International 167 (2), 845–852.

MONA LISA Working Group, 1997. MONA LISA — deep seismic investigations of the lithosphere in the southeastern North Sea. Tectonophysics 269, 1–19.

Morozova, E.A., Morozov, I.B., Smithson, S.B., Solodilov, L., 2000. Lithospheric boundaries and upper mantle heterogeneity beneath Russian Eurasia: evidence from the DSS profile QUARTZ. Tectonophysics 329 (1–4), 333–344.

Nettles, M., Dziewonski, A.M., 2008. Radially anisotropic shear velocity structure of the upper mantle globally and beneath North America. Journal of Geophysical Research—Solid Earth 113 (B2), B02303. doi:10.1029/2006JB004819.

Nishimura, C., Forsyth, D., 1989. THe anisotropic structure of the upper mantle in the Pacific. Geophysics Journal of the Royal Astronomical Society 96, 203–229.

Oreshin, S., Vinnik, L., Peregoudov, D., Roecker, S., 2002. Lithosphere and asthenosphere of the Tien Shan imaged by S receiver functions. Geophysical Research Letters 29 (8), 1191. doi:10.1029/2001GL014441.

Ozacar, A.A., Gilbert, H., Zandt, G., 2008. Upper mantle discontinuity structure beneath East Anatolian Plateau (Turkey) from receiver functions. Earth and Planetary Science Letters 269 (3–4), 426–434.

Pavlenkova, G.A., Priestley, K., Cipar, J., 2002. 2D model of the crust and uppermost mantle along rift profile, Siberian craton. Tectonophysics 355 (1–4), 171–186.

Peltier, W.R., Drummond, R., 2008. Rheological stratification of the lithosphere: a direct inference based upon the geodetically observed pattern of the glacial isostatic adjustment of the North American continent. Geophysical Research Letters 35 (L16314). doi:10.1029/2008GL034586.

Revenaugh, J., Sipkin, S.A., 1994. Mantle discontinuity structure beneath China. Journal of Geophysical Research—Solid Earth 99 (B11), 21,911–21,927.

Ryberg, T., Wenzel, F., Mechie, J., Egorkin, A., Fuchs, K., et al., 1996. Two-dimensional velocity structure beneath northern Eurasia derived from the super long-range seismic profile Quartz. Bulletin of the Seismological Society of America 86 (3), 857–867.

Rychert, C.A., Shearer, P.M., 2009. A global view of the lithosphere–asthenosphere boundary. Science 324 (5926), 495–498.

Rychert, C.A., Fischer, K.M., Rondenay, S., 2005. A sharp lithosphere–asthenosphere boundary imaged beneath eastern North America. Nature 436 (7050), 542–545.

Rychert, C.A., Rondenay, S., Fischer, K.M., 2007. P-to-S and S-to-P imaging of a sharp lithosphere–asthenosphere boundary beneath eastern North America. Journal of Geophysical Research—Solid Earth 112 (B08314). doi:10.1029/2006JB004619.

Rychert, C.A., Fischer, K.M., Abers, G.A., Plank, T., Syracuse, E., et al., 2008. Strong along-arc variations in attenuation in the mantle wedge beneath Costa Rica and Nicaragua. Geochemistry Geophysics Geosystems 9 (Q10S10). doi:10.1029/2008GC002040.

Saul, J., Kumar, M., Sarkar, D., 2000. Lithospheric and upper mantle structure of the Indian Shield, from teleseismic receiver functions. Geophysical Research Letters 27 (16), 2357–2360.

Savage, B., Silver, P.G., 2008. Evidence for a compositional boundary within the lithospheric mantle beneath the Kalahari craton from S receiver functions. Earth and Planetary Science Letters 272 (3–4), 600–609. doi:10.1016/j.epsl.2008.05.026.

Schutt, D.L., Lesher, C.E., 2006. Effects of melt depletion on the density and seismic velocity of garnet and spinel lherzolite. Journal of Geophysical Research—Solid Earth 111 (B5), B05401. doi:10.1029/2003JB002950.

Shearer, P.M., 1991. Constraints on upper mantle discontinuities from observations of long-period reflected and converted phases. Journal of Geophysical Research—Solid Earth 96 (B11), 18,147–18,182.

Simons, F.J., Zielhuis, A., van der Hilst, R.D., 1999. The deep structure of the Australian continent from surface wave tomography. Lithos 48 (1–4), 17–43.

Snyder, D.B., 2008. Stacked uppermost mantle layers within the Slave craton of NW Canada as defined by anisotropic seismic discontinuities. Tectonics 27 (4), TC4006. doi:10.1029/2007TC002132.

Sodoudi, F., Yuan, X., Liu, Q., Kind, R., Chen, J., 2006a. Lithospheric thickness beneath the Dabie Shan, central eastern China from S receiver functions. Geophysical Journal International 166 (3), 1363–1367.

Sodoudi, F., Kind, R., Hatzfeld, D., Priestley, K., Hanka, W., et al., 2006b. Lithospheric structure of the Aegean obtained from P and S receiver functions. Journal of Geophysical Research—Solid Earth 111 (B12307). doi:10.1029/2005JB003932.

Sodoudi, F., Yuan, X., Kind, R., Heit, B., Sadidkhouy, A., 2009. Evidence for a mising crustal root and a thin lithosphere beneath the Central Alborz by receiver function studies. Geophysical Journal International 177 (2), 733–742. doi:10.1111/j.1365-246X.2009.04115.x.

Steer, D.N., Knapp, J.H., Brown, L.D., Echtler, H.P., Brown, D.L., et al., 1998. Deep structure of the continental lithosphere in an unextended orogen: an explosive-source seismic reflection profile in the Urals (Urals Seismic Experiment and Integrated Studies (URSEIS 1995)). Tectonics 17 (2), 143–157.

Takei, Y., 2002. Effect of pore geometry on V-P/V-S: from equilibrium geometry to crack. Journal of Geophysical Research—Solid Earth 107 (B2), 2043. doi:10.1029/2001JB000522.

Takei, Y., Holtzman, B., 2009. Viscous constitutive relations of solid–liquid composites in terms of grain boundary contiguity: 1. Grain boundary diffusion control model. Journal of Geophysical Research—Solid Earth 114 (B06205). doi:10.1029/2008JB005850.

Tan, Y., Helmberger, D.V., 2007. Trans-Pacific upper mantle shear velocity structure. Journal of Geophysical Research—Solid Earth 112 (B08301). doi:10.1029/2006JB004853.

Thybo, H., 2006. The heterogeneous upper mantle low velocity zone. Tectonophysics 416 (1–4), 53–79.

van der Lee, S., 2002. High-resolution estimates of lithospheric thickness from Missouri to Massachusetts, USA. Earth and Planetary Science Letters 203 (1), 15–23.

Vinnik, L., Farra, V., 2002. Subcratonic low-velocity layer and flood basalts. Geophysical Research Letters 29 (4), 1049. doi:10.1029/2001GL014064.

Vinnik, L., Kumar, M.R., Kind, R., Farra, V., 2003. Super-deep low-velocity layer beneath the Arabian plate. Geophysical Research Letters 30 (7), 1415. doi:10.1029/2002GL016590.

Vinnik, L.P., Farra, V., Kind, R., 2004. Deep structure of the Afro-Arabian hotspot by S receiver functions. Geophysical Research Letters 31 (11), L11608. doi:10.1029/2004GL019574.

Vinnik, L.P., Foulger, G.R., Du, Z., 2005. Seismic boundaries in the mantle beneath Iceland: a new constraint on temperature. Geophysical Journal International 160 (2), 533–538.

Wittlinger, G., Farra, V., 2007. Converted waves reveal a thick and layered tectosphere beneath the Kalahari super-craton. Earth and Planetary Science Letters 254 (3–4), 404–415.

Wolbern, I., Jacob, A.W.B., Blake, T.A., Kind, R., Li, X., et al., 2006. Deep origin of the Hawaiian tilted plume conduit derived from receiver functions. Geophysical Journal International 166 (2), 767–781.

Yuan, X.H., Kind, R., Li, X.Q., Wang, R.J., 2006. The S receiver functions: synthetics and data example. Geophysical Journal International 165 (2), 555–564.

Zaranek, S., Parmentier, E., Fischer, K., 2005. Roles of small-scale convection, crustal heating, and basal motions in the evolution of the subcratonic lithosphere. Eos Transactions AGU 86 (52) Fall Meet. Suppl., Abstract T22C-05.